Investigation of nonlinear wave-induced seabed response around mono-pile foundation

Zaibin Lin[a], Dubravka Pokrajac [b], Yakun Guo [c], Dong-sheng Jeng [d], Tian Tang[e], Nick Rey[f] , Jinhai Zheng[g,h], Jisheng Zhang[g,h]

a. School of Engineering, University of Aberdeen, AB24 3UE, UK,
Corresponding author: zaibin.lin@gmail.com
b. School of Engineering, University of Aberdeen, AB24 3UE, UK
c. School of Engineering, University of Bradford, BD7 1DP, UK,
d. Griffith School of Engineering, Griffith University Gold Coast Campus, Queensland 4222, Australia
e. Bekaert Technology Center, Bekaert Company, Zwevegem, Belgium
f. Wood Group Kenny, Aberdeen, UK
g. College of Harbour, Coastal and Offshore Engineering, Hohai University, Nanjing 210098, China
h. Key Laboratory of Coastal Disaster and Defence（Hohai University），Ministry of Education，Nanjing 210098, China

Abstract: Stability and safety of offshore wind turbines with mono-pile foundations, affected by nonlinear wave effect and dynamic seabed response, are the primary concerns in offshore foundation design. In order to address these problems, the nonlinear wave effect on dynamic seabed response in the vicinity of mono-pile foundation is investigated using an integrated model, developed using OpenFOAM, which incorporates both wave model (waves2Foam) and Biot's poro-elastic model. The present model was validated against several laboratory experiments and promising agreements were obtained. Special attention was paid to the systematic analysis of pore water pressure as well as the momentary liquefaction in the proximity of mono-pile induced by nonlinear wave effects. Various embedment depths of mono-pile relevant for practical engineering design were studied in order to attain the insights into nonlinear wave effect around and underneath the mono-pile foundation. By comparing time-series of water surface elevation, inline force, and wave-induced pore water pressure at the front, lateral, and lee side of mono-pile,

the distinct nonlinear wave effect on pore water pressure was shown. Simulated results confirmed that the presence of mono-pile foundation in a porous seabed had evident blocking effect on the vertical and horizontal development of pore water pressure. Increasing embedment depth enhances the blockage of vertical pore pressure development and hence results in somewhat reduced momentary liquefaction depth of the soil around the mono-pile foundation.

Key words: wave-structure-seabed interaction (WSSI); dynamic seabed response; mono-pile foundation; blockage effect; momentary liquefaction

1. Introduction

Demand for green energy in response to climate change has driven a substantial increase of construction of offshore wind farms in the past decades, which is likely to continue in the forthcoming years. Large diameter mono-pile is the preferred foundation for offshore wind turbines located in shallow or intermediate water depths. Mono-pile foundation supporting offshore wind turbine may suffer the damage from strongly nonlinear, and even breaking waves. The soil near a mono-pile foundation may be liquefied under wave loading and in turn aggravate the vibration of the offshore wind turbine. Understanding these mechanisms and accurate prediction of their influences on mono-pile foundations are therefore particularly important in engineering design.

In recent decades, wave-induced hydrodynamic loads acting on the cylindrical structure have been extensively studied since they are of primary concern in offshore engineering. The costly and time-consuming laboratory experiments cannot provide a complete set of results on wave-structure interaction. Consequently, the numerical models of wave-structure interaction have been increasingly used. Based on potential theory and the assumption that flow is inviscid and irrotational, various numerical analyses of linear and weakly non-linear wave-structure interactions have been presented. To study the three-dimensional (3D) wave-structure interaction, Ma et al. (2001a, 2001b) numerically solved the fully nonlinear potential flow with Finite Element Method (FEM) incorporating recovery technique to obtain better solution. The same approach was used by Kim et al. (2006) to investigate wave run-up around cylinders with steeper Stokes waves. The technique of

domain decomposition with enforcing continuity of the interface between neighbour subdomains was implemented by Bai and Taylor (2007, 2009) to examine fully nonlinear wave interaction with vertical cylinder. However, the potential flow theory is limited to non-breaking and small steepness waves (small H/L, where H is the wave height, and L is the wave length). The alternative that is becoming increasingly popular is to use Computational Fluid Dynamics (CFD) for investigating high steepness wave interacting with offshore structures, including breaking wave effect and higher-order harmonic forces. Recent CFD computations within the framework of OpenFOAM based on Finite Volume Method (FVM), a free access source C++ library for various fluid flow and solid mechanics problems, have been performed to obtain the insights into fully nonlinear wave-structure interactions. Using the wave generation tool waves2Foam (Jacobsen et al., 2012), Paulsen et al. (2014b) investigated the capacity of OpenFOAM for modelling nonlinear wave motion interacting with mono-pile foundation for a range of Keulegan–Carpenter (KC) numbers, $KC = U_m T/D$, where U_m is the maximum velocity, T is wave period and D is the diameter of cylinder (Sumer and Fredsøe, 2006), and concluded that the dominant physics of wave-pile interactions was well predicted, despite the simplification of cylinder wall and the seabed surface boundary conditions. Paulsen et al. (2014a) introduced an innovative domain decomposition approach to integrate potential flow theory model (OceanWave3D) developed by Engsig-Karup et al. (2009) and waves2Foam library (Jacobsen et al., 2012) based on Navier-Stokes (NS) equations and volume of fluid method (VOF). Good agreement between numerical and experimental results has been obtained for several sensitivity tests of wave loads on a cylindrical pile foundation. A comprehensive investigation of the potential of OpenFOAM for accurately predicting the interactions between wave and vertical cylinder was elaborated by Chen et al. (2014) for a variety of wave conditions, including regular and focused waves. Higuera et al. (2013a) developed an advanced wave generation tool and the active wave absorption boundary condition (IHFOAM) for predicting wave interaction with coastal structures in coastal engineering (Higuera et al., 2013b; Higuera et al., 2014a; Higuera et al., 2014b). A moving boundary condition with multi-paddles for wave generation is further incorporated into IHFOAM (Higuera et al., 2015) together with an improved active wave absorption boundary. Nevertheless, the research solely concerning the mechanism of wave interacting with offshore structure does not fully cover the complexity of realistic design issues.

Another important issue in offshore engineering is the risk associated with formation of liquefied zone of seabed as a consequence of wave-induced dynamic seabed response in the vicinity of offshore structures (Sumer, 2014; Sumer and Fredsøe, 2002； Ye et al., 2016; Ye et al., 2015). Liquefaction can be caused by two different mechanisms which occur at different time-scales, so we distinguish between residual and momentary liquefaction. Residual liquefaction typically occurs in undrained soils, when the pore water pressure accumulated over time exceeds overburden pressure (Sumer, 2014). A much shorter-lived phenomenon, termed momentary liquefaction, occurs in an unsaturated seabed, due to the direct effect of wave pressure imposed on seabed surface under wave trough. The resulting fast decrease of pore water pressure in the unsaturated seabed generates large upwards pressure gradients. If the lift induced by upward gradient of pore water pressure surpasses the submerged weight of soil, effective stress vanishes and the soil is liquefied. From geotechnical aspect, the occurrence of liquefaction under extreme wave impact during storm conditions may result in the failure of the supporting foundation of an offshore structure, as well as foundation protection. The relationship between momentary liquefaction and extreme wave interaction with mono-pile foundation is the primary focus of present study.

In past decades, the analytical studies of wave-induced seabed response have also been extensively carried out. Madsen (1978) and Yamamoto et al. (1978) extended the poro-elastic Biot's theory (Biot, 1941) to a close-form analytical solution for the examination of wave-induced seabed response. Afterwards the investigation of wave-induced response for both coarse and fine sand, using a boundary-layer approximation, was conducted by Mei and Foda (1981). They pointed out that their approach can be used to economically solve poro-elastic boundary value problem with a free surface. Using a simpler analytical solution, Okusa (1985) studied wave-induced stability of completely or partially saturated seabed with a conclusion that Skempton's pore pressure coefficient played a key role in predicting wave-induced seabed response. Hsu and Jeng (1994) analytically derived a closed-form solution to investigate wave-induced soil response within the case of a finite thickness seabed. A good agreement was found between their results and semi-analytical solution (Yamamoto et al., 1978). After then, a thorough review on research of wave-induced dynamic seabed response

was described by Jeng (2003), where both theoretical and physical studies are included and examined in detail. Most recently, with the fully dynamic soil behaviour considered, Liao et al. (2013) presented an analytical study of combined effect of wave and current over an infinite seabed. It was noted that the effect of currents on the seabed response was significant only in the upper area closed to seabed surface (about 10% of wave length). Nevertheless, the aforementioned analytical investigations are limited to given assumptions and scenarios.

To improve understanding of the entire wave-induced seabed response multiple physical experiments were conducted with/without structures. Based on the laboratory experiments in a wave flume, Sumer et al. (2006) elaborated the mechanism of wave-induced liquefaction and consecutive compaction of a flat seabed without structures, and suggested that the completion of compaction and final equilibrium with continuing waves produces ripples. The laboratory experiments of Sumer et al. (2007) confirmed that when the progressive wave was greater than critical wave height, the soil around a pile, that was freshly settled without liquefaction history, may experience liquefaction after installation. In the dense-silt scour tests, it was also demonstrated that the scour around the pile may occur after liquefaction and compaction. Liu et al. (2015) conducted one-dimensional (1D) soil column experiments to investigate wave-induced pore water pressure in various sandy soil conditions. The soil thickness was found to decrease due to the dynamic loading. Though the realistic mechanism of wave-induced seabed response is easily captured by using natural materials, physical experiments are relatively expensive to carry out and restricted to the limited-scale cases.

Numerical modelling has been broadly employed as a cost-effective method for investigating seabed response induced by various wave conditions. Li et al. (2011) used FEM approach to numerically solve the 3D Biot's equations without considering wave diffraction in their model. Wave-induced seabed response around pile foundation, including transient and residual pore water pressure, was examined for different pile diameters. However, in this study, the incident wave was simplified as an analytical solution, so that the complicated wave-structure interaction was not taken into consideration. The rapid development of computing resources enables researchers to couple flow model with seabed model into an integrated model, which enables them to systematically investigate

the mechanisms of seabed response to waves in the vicinity of offshore structures, such as pipelines (Lin et al., 2016; Zhao et al., 2016a; Zhao et al., 2016b; Zhao et al., 2014) and breakwaters (Jeng et al., 2013; Jianhong et al., 2014; Jianhong et al., 2013; Ye et al., 2013a; Ye et al., 2013b). In the previous studies, the equations governing fluid and soil behaviour were solved by different methods, namely flow field by FVM and soil model by FEM. A monolithic approach to both models was used in Lin et al. (2016), who developed an integrated FEM Wave-Seabed-Structure Interaction (WSSI) model to explore the wave-induced liquefaction potential in the vicinity of a partially/fully buried pipeline in an open trench. As an alternative approach, Liu et al. (2007) first discretized the Biot's equations in a FVM manner within OpenFOAM, and then investigated the wave-induced response around the submerged object without parallel computing. Tang et al. (2015) and Tang (2014) extended and modified the poro-elastic Biot's model to poro-elasto-plasticity soil model. However, so far majority of integrated models have focused on the investigation of wave-pipeline/breakwater-seabed interaction. For the wave-pile-seabed interaction, a numerical study based on FVM-FEM approach carried out by Chang and Jeng (2014) showed that replacing the soil around a high-rising structure foundation was an effective protection against liquefaction. The only available numerical model of WSSI focuses solely on the dynamic seabed response induced by weakly nonlinear waves or regular non-breaking waves. Recently, Sui et al. (2015) integrated FUNWAVE (Kirby et al., 2003; Shi et al., 2001; Wei and Kirby, 1995) and fully dynamic (FD) form of Biot's equations to investigate the small steepness wave-induced seabed response around mono-pile without considering fully nonlinear wave-pile interaction. In their study, dynamic response of porous seabed, structural dynamics of mono-pile, and their interactions were all solved by FD form of Biot's equations. However, the nonlinear wave-pile interaction has a significant effect on porous seabed response. This complex process is not fully studied in the aforementioned studies. Consequently, an integrated WSSI numerical model capable of accurately estimating strongly nonlinear wave load and the corresponding dynamic seabed response provides an efficient tool for the design of offshore wind turbine foundations.

This paper presents a sophisticated WSSI numerical model developed in order to aid the design for offshore wind turbine foundations. A segregated FVM solver is implemented within the framework

of OpenFOAM, incorporating waves2Foam and Biot's equations, to address the issue of nonlinear wave-induced dynamic seabed response surrounding mono-pile foundation. The description of wave and seabed model is outlined in Section 2. Section 3 presents the validation of present model against several available experimental data sets. In Section 4 the calibrated model is used to investigate the nonlinear wave-induced dynamic seabed response, as well as the liquefaction potential, around mono-pile foundation. The main conclusions are listed in Section 5.

2. Numerical model

Figure 1 shows a sketch of simulation domain for the WSSI numerical model developed in this study. The domain includes two sub-domains: the sea water (including the air above the free surface) and the porous bed. The two corresponding sub-models, namely waves2Foam (Jacobsen et al., 2012) and QS (quasi-static) Biot's model, are integrated into the present WSSI model. The flow field is described by the incompressible Navier-Stokes equations with water-air interface traced by Volume of Fluid method (Berberović et al., 2009; Hirt and Nichols, 1981). The dynamic behaviour of a porous seabed is governed by QS Biot's equations, which contain both the pore water pressure and soil displacement. The process of integration is implemented by extended general grid interpolation (GGI), which interpolates the face and point from zone to zone for non-conformal meshes at the wave-seabed interface (Tukovic et al., 2014).

2.1 Wave model

The governing equations for simulating two-phase incompressible flow dynamics are

$$\nabla \cdot \boldsymbol{u} = 0 \tag{1}$$

$$\frac{\partial \rho \boldsymbol{u}}{\partial t} + \nabla \cdot (\rho \boldsymbol{u}) \boldsymbol{u}^{\mathrm{T}} = -\nabla p^{*} - (\mathbf{g} \cdot \boldsymbol{x}) \nabla \rho + \nabla \cdot (\mu \nabla \boldsymbol{u}) \tag{2}$$

$$\frac{\partial \alpha}{\partial t} + \nabla \cdot \boldsymbol{u} \alpha + \nabla \cdot \boldsymbol{u}_{r} \alpha (1 - \alpha) = 0 \tag{3}$$

where $\boldsymbol{u}$ is velocity field; ρ is fluid density; t is time; $p^{*} = p - \rho \mathbf{g} \cdot \boldsymbol{x}$ is the modified pressure which removes the effect of static pressure from the momentum equation (2); $\mathbf{g}$ and $\boldsymbol{x}$ are gravity acceleration and Cartesian coordinate vector, respectively; p is total pressure; μ is dynamic viscosity; $\boldsymbol{u}_{r}$ is relative velocity field (Berberović et al., 2009); α is scalar field of volume fraction

function. α is equivalent to 1 when the computational cell indicates water field, while $\alpha = 0$ indicates the simulated field to be air, and the water-air mixture field is denoted by $0 < \alpha < 1$. The momentary flow density and dynamic viscosity are computed by following equations:

$$\rho = \alpha\rho_w + \rho_a(1-\alpha) \tag{4}$$

$$\mu = \alpha\mu_w + \mu_a(1-\alpha) \tag{5}$$

where the sub-indices *w* and *a* represent water and air, respectively.

Consistently with the investigation by Paulsen et al. (2014b), where boundary layer effects were not taken into consideration, slip boundary condition is specified on the seabed, mono-pile surface, and lateral boundaries of the numerical wave flume. The atmospheric boundary at the upper boundary of flow domain is selected as a pressure outlet condition. The more comprehensive description of wave generation (inlet boundary) and wave absorption (outlet boundary) zone can be found in Jacobsen et al. (2012).

2.2 Seabed model

In present study, QS Biot's equations (Biot, 1941) are adopted as the governing equations for describing wave-induced dynamic soil response in a hydraulically isotropic porous seabed. The combined continuity and motion equation for the pore water is:

$$\nabla^2 p_p - \frac{\gamma_w n_s \beta_s}{k}\frac{\partial p_p}{\partial t} = \frac{\gamma_w}{k}\frac{\partial \varepsilon_s}{\partial t} \tag{6}$$

where p_p is wave-induced pore water pressure (i.e. pore water pressure in excess of the static pressure due to mean seawater level); γ_w is the unit weight of pore water; n_s is soil porosity; k is the Darcy's permeability assumed to be the same in all directions. The compressibility of pore fluid β_s and the volume strain ε_s are defined by

$$\beta_s = \frac{1}{K_w} + \frac{1-S_r}{P_{w0}} \tag{7}$$

$$\varepsilon_s = \nabla \cdot \boldsymbol{v} = \frac{\partial u_s}{\partial x} + \frac{\partial v_s}{\partial y} + \frac{\partial w_s}{\partial z} \tag{8}$$

where K_w is the bulk modulus of pore water (adopted as 2×10^9 N/m^2 in Section 3.2, Yamamoto et al., 1978, and 2.3×10^9 N/m^2 in Section 4, Hansen, 2012); S_r is soil saturation degree; P_{w0} is absolute static water pressure; $\boldsymbol{v} = (u_s, v_s, w_s)$ is soil displacement vector.

The force equilibrium in a poro-elastic seabed can be calculated via following equation:

$$G\nabla^2 \boldsymbol{v} + \frac{G}{1-2\nu}\nabla\varepsilon_s = \nabla p_p \tag{9}$$

where G is the shear modulus of soil and can be obtained through Young's modulus (E) and Poisson's ratio (ν):

$$G = \frac{E}{2(1+\nu)} \tag{10}$$

Hansen (2012) suggested that Young's modulus (E) for the soil at large depth within a seabed can be determined by

$$E = E_{ref}\left(\frac{\sigma_3'}{\sigma_{3,ref}'}\right)^{\alpha} \tag{11}$$

where E_{ref} is reference Young's modulus of soil, σ_3' and $\sigma_{3,ref}'$ are confining pressure and reference confining pressure, respectively, α is a constant ranging from 0.5 to 0.7 for sand.

In accordance with the generalized Hooke's law, effective normal stress, σ_i', and shear stress, τ_{ij}, where the subscripts $i,j=x,y,z$ indicate the direction of Cartesian coordinate, can be determined by

$$\sigma_x' = 2G\left(\frac{\partial u_s}{\partial x} + \frac{\nu}{1-2\nu}\varepsilon_s\right),\ \sigma_y' = 2G\left(\frac{\partial v_s}{\partial y} + \frac{\nu}{1-2\nu}\varepsilon_s\right) \tag{12}$$

$$\sigma_z' = 2G\left(\frac{\partial w_s}{\partial z} + \frac{\nu}{1-2\nu}\varepsilon_s\right), \tau_{xy} = \tau_{yx} = G\left(\frac{\partial u_s}{\partial y} + \frac{\partial v_s}{\partial x}\right) \tag{13}$$

$$\tau_{xz} = \tau_{zx} = G\left(\frac{\partial u_s}{\partial z} + \frac{\partial w_s}{\partial x}\right), \tau_{yz} = \tau_{zy} = G\left(\frac{\partial v_s}{\partial z} + \frac{\partial w_s}{\partial y}\right) \tag{14}$$

Several boundary conditions have to be specified at the boundary of seabed domain and the pile-seabed interface for an accurate prediction of WSSI. At seabed surface, y=0 (Fig. 1), the wave-induced pore water pressure, p_p, is set equal to p^* obtained from the wave model, and vertical effective normal stress and shear stresses are considered to be 0,

$$\sigma_z' = \tau_{xy} = \tau_{yz} = 0,\ p_p = p^* \text{ at y = 0} \tag{15}$$

At the bottom of seabed (y = -h_s, where h_s is soil depth, Fig. 1), an impermeable rigid boundary condition is applied, where soil displacement is zero and there is no vertical flow:

$$u_s = v_s = w_s = \frac{\partial p_p}{\partial y} = 0 \text{ at } y = -h_s \tag{16}$$

The same no flow (zeroGradient) and zero soil displacement boundary condition is applied at the lateral boundaries (Chang and Jeng, 2014):

$$u_s = v_s = w_s = \frac{\partial p_p}{\partial x} = 0 \quad \text{at } x = 0 \text{ and } x = L_s \tag{17}$$

$$u_s = v_s = w_s = 0, \ \frac{\partial p_p}{\partial z} = 0 \quad \text{at } z = -W_s/2 \text{ and } z = W_s/2 \tag{18}$$

In order to eliminate the influence of lateral boundaries, the length, L_s, and the width, W_s, of simulation domain (Fig. 1), were taken as four times the wavelength, L_w, and sixteen times the mono-pile diameter D. This domain size was used in Chen et al. (2014) to investigate wave-structure interaction. It is reported in Ye and Jeng (2012) that the soil domain length (L_s) larger than double wavelength is sufficient to eliminate the impact from fixed lateral boundaries. Thus, the mono-pile is located at the centre of computing domain and the lateral boundary of soil domain does not affect the simulated results around mono-pile foundation. Additionally, mono-pile is simulated as a rigid impermeable object so that at its surface the no-flow boundary condition applies, i.e. the gradient of pore water pressure vanishes:

$$\frac{\partial p_p}{\partial n} = 0 \tag{19}$$

where n denotes the normal to mono-pile surface. This boundary condition is acceptable for the rigid object located within a porous seabed (Chang and Jeng, 2014; Lin et al., 2016; Zhao et al., 2016a).

2.3 Integration process between wave and seabed model

Unlike the previous two-dimensional (2-D) monolithically integrated model in COMSOL Multiphysics using FEM (Lin et al., 2016), the three-dimensional (3-D) one-way integrated WSSI model is proposed in OpenFOAM with FVM. The present integrated model is able to simulate the wave-structure interaction more accurately, with low-cost of computer memory, and with high mesh density in the 3-D case. It solves the wave and soil model by two steps within one time step as illustrated in Fig. 2. First of all, in accordance with input wave parameters and the adjustable time step calculated by Courant–Friedrichs–Lewy (CFL) condition (adopted as 0.5 in this study), the wave model solves the Navier-Stokes and Volume of Fluid equations by the combined algorithm (PISO-SIMPLE, namely PIMPLE) for pressure-velocity coupling. Secondly, the dynamic wave pressure is extracted from wave model and applied to seabed surface through extended general grid

interpolation (GGI) (Tukovic et al., 2014), which allows the integrated model to run WSSI computation in parallel within a time step compared to the serial WSSI simulation in Liu et al. (2007). The soil model then computes the wave-induced dynamic seabed response by solving QS Biot's equations using FVM method (Tang and Hededal, 2014). After the completion of two sub-models simulations within a time step, the integrated model exports the simulated results based on pre-set writing time interval and then continues to the next time step simulation until the prescribed total simulation time is reached.

3. Validation

In this section, we validate both wave and seabed components of the integrated WSSI model against the available published laboratory experimental results. The lateral and plan views of numerical domains are shown in Fig. 1. The wave characteristics and soil properties used for validation are listed in Table 1.

3.1. Wave model

Before applying the present WSSI to practical engineering, the ability of model to accurately simulate wave nonlinearity when interacting with a mono-pile needs to be investigated. The experimental data presented in Chen et al. (2014) and Zang et al. (2010) are adopted to validate present wave model. Two types of regular wave, one with the wave height H = 0.14 m, and the wave period T =1.22 s, and another one with H = 0.12 m, T =1.63 s, are used to study the nonlinear wave-structure interaction. To reproduce the laboratory experiment a 3-D numerical wave tank was established, as shown in Fig. 1, but without seabed sub-domain. In laboratory experiment, the diameter of mono-pile, D, is 0.25 m, while mean water depth, h_w, is 0.505 m. On the basis of the investigation of mesh sensitivity by Paulsen et al. (2014b), the refined mesh with a resolution of 15 points per wave height is adopted in the validation.

Fig. 1 also shows several wave gauges and pore water pressure sensors locations for model validations and further applications in the numerical wave-seabed tank. Wave gauge 1 at 0.77 m from the inlet, and Wave gauge 2 at 0.002 m distance from the upstream mono-pile surface along the

centreline are used to measure free surface elevation, η. Fig. 3 (a) shows the comparison of simulated and experimental free surface elevation for the incident wave, i.e. at Wave gauge 1. The simulated incident wave is in a good agreement with the experimental results. The time series of simulated and experimental free surface level close to the mono-pile (at Wave gauge 2) for two different regular waves are shown in Fig. 3(b) and 3(c). Excellent agreement between numerical and experimental results denote that present wave model has the capacity to simulate the strongly nonlinear behaviour of waves interacting with mono-pile, including the small jump after wave troughs.

The simulated wave-induced inline force on the surface of mono-pile, F_x, is also compared with experimental results in Fig. 4. The simulated inline force is calculated by spatial integration of the total pressure, p, over the surface of the mono-pile exposed to sea water (the water sub-domain in Fig. 1). Despite minor discrepancy at wave nodes the agreement between computed and experimental results is generally good, hence showing that the application of present wave model to practical engineering is promising. The aforementioned validations show that nonlinearity of wave-pile interaction is accurately predicted in the numerical wave tank in both cases. It can be concluded that present wave model (waves2Foam) is capable of capturing the nonlinear wave-pile interactions, including free surface elevation and wave load on the mono-pile.

3.2. Wave-seabed interaction model

Wave-induced dynamic seabed response was validated by comparison of simulation results with the laboratory experiment of Liu et al. (2015). The laboratory experiment was carried out in a one-dimensional column filled with sand saturated with water, and exposed to a periodic variation of pressure at the cylinder top. The time series of the resulting variation of pore water pressures was measured at several locations along the column. The soil properties used for validation are listed in Table 1 and the reader is referred to Liu et al. (2015) for more details. In order to eliminate the potential effect from lateral boundaries, the soil domain for validating soil model is designed as a 2-D case, in which the lateral and bottom boundary conditions are selected as demonstrated in section 2.2, and at seabed surface, analytical wave pressure based on laboratory experiment is

imposed. The soil properties tabulated in Table 1 are measured in Liu et al. (2015), and then used as input parameters in the validation of soil model.

Vertical distribution of wave-induced pore water pressure from the experiment shown in Liu et al. (2015) is compared with numerical simulation in Fig. 5. Results are scaled with the maximum pore water pressure at seabed surface, P_0. The simulated results generally agree with the experiment and the analytical result (Hsu and Jeng, 1994) except for an obvious discrepancy at the position close to seabed bottom (y/h_s=-0.8). A possible explanation, given in Liu et al. (2015), is that the soil in the physical test was not perfectly homogeneous, i.e. soil properties could have been different close to the bottom, while in numerical model soil properties are constant. The time series of wave-induced pore water pressure at the depth y = -0.067 m (y/h_s=-0.037) against experimental data is shown in Fig. 6, in which ω is wave frequency. The numerical prediction agrees well with the experimental results. In conclusion we are confident that the present seabed model in OpenFOAM has the capacity to accurately model the wave-induced dynamic seabed response.

4. Application

In reality, the foundations of offshore mono-piles are protected by granular filters in order to prevent scour which may result in the failure of the offshore structures. As pointed out by Kirca (2013), the seabed beneath granular filters may experience liquefaction in the seabed below. Following the satisfactory validations present coupled WSSI model is further applied to investigate dynamic seabed response in the proximity of mono-pile foundation due to nonlinear effect of wave-pile interaction at intermediate water depth. In this example, the wave from the Danish 'Wave loads' project (Paulsen et al., 2014b) is considered, and the wave field interacts with a mono-pile of 6 m diameter (D). The mean water depth is constant, h_w = 20 m. The detailed wave and seabed parameters for investigation of nonlinear wave-induced seabed response around mono-pile are listed in Table 2. To determine the distribution of Young's modulus (E) in seabed, E_{ref} = 177 MPa, $\sigma'_{3,ref}$ = 150 kPa, and α = 0.62 are used in accordance with the medium sand in Eskesen et al. (2010). In reality the vibration of mono-pile due to the action of violent wave may compact granular soil and urge the air out, leading to a denser and more saturated soil around mono-pile foundation during pile vibration. In present

study this phenomenon is not simulated - mono-pile is assumed to be very rigid and the seabed saturation is adopted as a constant (Table 2). The focus of present study is therefore solely on dynamic behaviour of porous seabed and associated potential liquefaction around mono-pile foundation caused by the interaction of extreme wave and mono-pile foundation.

The initial investigation is performed for a mono-pile that is embedded into seabed until the depth equal triple pile diameter. We first examine the connection between nonlinear wave and dynamic seabed response due to the blockage effect of mono-pile. According to the available momentary liquefaction criterion, the potential momentary liquefaction zone around mono-pile is studied in detail. The final part of this study investigates the influence of the embedment depth of mono-pile foundation, ranging from three to seven times pile diameter, on the dynamic seabed response to the action of high steepness waves.

4.1 Vertical distribution of pore water pressure in the vicinity of mono-pile

The vertical distribution of pore water pressure around pile is recorded at a series of vertical profiles located 0.05 m away from the surface of mono-pile with θ ranging from 0° to 180° with 45° increment (wave gauges 2-6 in Fig. 1), and at position 7 located in the centre of mono-pile. The corresponding vertical profiles of pore water pressures are shown in Fig. 7 with t/T varying from 5.04 to 6.07, i.e. over one period. In general, the vertical distribution of pore water pressure has the greatest amplitudes at front face of mono-pile foundation, θ = 0°, and the smallest amplitudes at θ = 90°. Between θ=0° and θ=90°, the overall pore water pressures along embedment depth reduce, while beneath the pile there is only a slight decrease. For θ between 90° and 180°, the trend reverses, resulting in peak pressures at θ =180°. The reason for these trends may be a consequence of free surface elevation variation together with the variation of wave pressure around mono-pile. The comparison and analysis of relationship between wave-pile interaction and pore water pressure distribution are elaborated in next section.

As shown by Zhang et al. (2015), the presence of mono-pile in seabed increases the pore water pressure along mono-pile foundation compared to that without mono-pile foundation penetrated into

seabed. Fig. 7(a)-(e) shows that the magnitude of pore water pressure declines rapidly from the seabed surface to approximately y = -1.8 m, and then slightly decreases until the depth of about y = -17.46 m, close to the pile bottom. Between y = -17.46 m and y = -19 m, an evident fall of pore water pressure magnitude can be noticed. The explanation of this is that the soil below pile bottom may be shielded from the pore water pressure induced by propagating wave above. Fig. 7 (f) presents the pore water pressure along the central line of mono-pile bottom. In comparison with the pore water pressure around mono-pile circumference at y = -18 m, the pore water pressure underneath pile bottom is relatively small and has limited variation. The limited impact of the wave pressure on the dynamic soil response under pile bottom at different θ-locations also confirms the shielding effect of pile foundation.

4.2 Wave-induced seabed response around mono-pile

The wave model validation has shown (Fig. 3) that high steepness wave has an evident nonlinearity when interacting with mono-pile. Wave crest and wave trough, as well as pore water pressure, develop nonlinearly due to interaction with mono-pile, compared to the case without mono-pile. This is primarily due to the blockage effect of mono-pile in the wave and pore water pressure propagating direction.

In order to further examine the notable variation of pressure at several vertical locations, y = 0 m, -1.8 m, -17.46 m, and -18 m, the time histories of pore water pressure at these locations, as well as the time history of free surface elevation are presented in Fig. 8, at the same locations 0.05 m away from mono-pile surface (wave gauges 2-6 in Fig. 1). The t/T from 4 to 7, when the interaction of wave and mono-pile has attained the dynamic equilibrium, is considered. It can be noticed that the interaction between wave and mono-pile produces strong nonlinearity of free surface elevation, even wave-breaking at WG4 and WG5. This in turn affects pore water pressure, which shows similar albeit development history. By comparing free surface elevation at various wave gauges, it is implied that the maximum free surface elevation declines gradually with θ increasing from 0° to 135° and, at WG6 (θ = 180°), the maximum free surface elevation raises due to the merge of incident wave crest propagated separately from both lateral sides of pile (Swan and Sheikh, 2015). Pore water pressure

408 presents similar decrease when θ grows from 0° to 90°, but different development at θ = 135°. It can
409 be inferred that, when the free surface elevation is changing rapidly, the water pressure at the seabed,
410 and hence also pore water pressure within the bed, do not respond simultaneously. The precise
411 simulation of wave pressures around the pile is therefore required in order to accurately model the
412 dynamic seabed response.
413
414 The second column of Fig. 8, shows that, while pore water pressure at y = -1.8 m still shows similar
415 development history as that at seabed surface, the effect of wave-pile interaction on pore water
416 pressure becomes weaker as the observation point moves from -1.8 m to -18 m. The comparison of
417 maximum pore water pressure at different θ in Fig. 8 shows once more that the pore water pressure at
418 θ = 90° reaches its minimum.
419
420 4.3 Wave-induced liquefaction around pile
421 Liquefaction around offshore structures is considered as one of the primary threats to operational
422 lifetime of these structures (Sumer, 2014), so it is a major concern in the engineering practice. Based
423 on the liquefaction criterion suggested in Jeng (2013) and Sumer (2014), the potential liquefaction
424 zone can be determined by

$$-(\gamma_s - \gamma_w)y \leq (p_{ps} - P_b) \tag{20}$$

425 where γ_s and γ_w are the unit weight of seabed and water, respectively ($\gamma_s = 1.9\,\gamma_w$ was used in
426 this study); P_b is the pore water pressure on the seabed surface; p_{ps} is the pore water pressure
427 within porous seabed. Liquefaction may occur in a porous seabed when the net excessive pore water
428 pressure, equals to the difference between the pressure at seabed surface and pressure at a point
429 beneath the surface, surpasses overburden soil pressure and soil matrix begins to lose its capacity for
430 undertaking any load.
431
432 Using the aforementioned liquefaction criterion, maximum liquefied depth was evaluated and its
433 time series is shown in Fig. 9, along with free surface elevation and inline force. Comparison
434 between Fig. 9 (a) and (c) shows that the momentary liquefaction close to mono-pile surface takes
435 place periodically at the moment when free surface elevation at WG2 is smaller than 0 and inline

436 force has its minimum (see Fig. 9). As a consequence of the propagation of wave trough, liquefied
437 depth reaches its maximum. Maximum liquefaction depth drops and disappears due to the arrival of
438 wave crest and rapid increase of free surface elevation and excess pressure on seabed surface from
439 negative to positive, which in turn leads to decrease of the difference of pore water pressure at
440 seabed surface and within seabed, which can be observed at t/T = 5.33 to 5.92 in Fig. 7.
441
442 Comparison of Fig. 9 (b) and (c) in the case with *KC* number being 8.85 and D/L being 0.032, shows
443 that during the potential liquefaction period, very close to maximum depth, there is also negative
444 inline force directed upstream (F_x <0). As a result of this, the liquefied soil in the closest vicinity of
445 mono-pile loses its support and then may enlarge mono-pile vibration, which is induced by periodic
446 inline force. As mentioned earlier this periodic vibration of mono-pile foundation may pressurize
447 adjacent soil in the vibration direction, and force the air out. As a consequence this process tend to
448 harden surrounding soil and alter soil properties. For pile-seabed interaction, the reader is referred to
449 Hansen (2012) for more details. To avoid the threat from potential liquefaction around foundation,
450 Chang and Jeng (2014) suggested that momentary liquefaction may be prevented by replacing the
451 existing soil layer with coarse sand layer with greater permeability.
452
453 Further presentation of the extent of liquefaction potential is shown in Fig. 10 at t/T = 5.66, when
454 liquefaction depth is the largest (highlighted by black hollow circle in Fig. 9 (c). As shown in Fig. 10
455 (a) and (b), momentary liquefaction potential arises broadly while wave trough is approaching
456 mono-pile over porous seabed. Compared with the liquefaction zone without mono-pile in the far
457 field, liquefaction at front and back face of mono-pile foundation are relatively smaller. Fig. 10 (c)
458 shows the liquefaction depth at the interface between soil and foundation with θ ranging from 0° to
459 180°. The liquefaction depth is about 1 m at the front face of pile foundation; it gradually increases
460 as the observation point moves around the pile perimeter to reach maximum of approximately 1.5 m
461 at θ = 90°, and then slightly reduces as the point moves from θ = 90° and θ = 180°. The temporal
462 evolution of the liquefaction depth at several θ-locations along the pile perimeter are presented in Fig.
463 10 (d). The liquefaction first appears at front face of mono-pile foundation and then rapidly
464 approaches its lateral side (θ = 90°), where the maximum liquefaction depth occurs. Between the

lateral side and the back face there is further slight delay and slight decrease of the maximum liquefaction depth.

Momentary liquefaction in porous seabed propagates along with the wave trough above seabed. For the purpose of investigating possible threat from momentary liquefaction to scour protection, maximum potential liquefaction depth in the vicinity of mono-pile foundation over a wave period (t/T from 5 to 6) is presented in Fig. 11. It can be observed that maximum liquefaction depth of around 1.5m is located in the lateral zone near mono-pile foundation, with θ approximately ranging from 60° to 110°, while minimum potential liquefaction depth of approximately 1 m occurs at front and back side of mono-pile foundation, where θ equals 0° and 180°, respectively. It can be inferred that for KC = 8.85 and D/L = 0.032 the scour protection may experience greater liquefaction threat, which may cause it to sink, in the areas close to lateral sides of mono-pile foundation than in the areas close to the front and back side.

4.4 Influence of embedded depth

In reality, the ratios of embedment depth for mono-pile foundation of offshore wind turbine and mono-pile diameter often vary from 4 to 8 at shallow/intermediate water depth (Lesny et al., 2007). Therefore, for the same wave conditions listed in Table 2, the present model is further applied to the examples with two additional embedment depths, namely 30 m and 42 m (Table 2), in order to investigate the effects of embedment depth on the development of pore water pressure and potential liquefaction.

Figures 12 and 13 show the development of vertical distribution of pore water pressure for the embedment depth of 30 m and 42 m respectively. For both cases the development of pore water pressure along embedment depth, as well as along pile bottom are similar to those already shown in Fig. 7 (section 4.1), for the main case with the embedment depth of 18m. The development of the vertical pressure profiles around the pile perimeter is also similar for the three cases: pore water pressure declines as θ grows from 0° to 90° and then raises with θ ranging from 90° to 180°. However, the magnitude of pore water pressure along the foundation reduces as the embedment

494 depth grows.

495

496 The estimated liquefaction depths in the aforementioned examples with 3 various penetration depths
497 are shown in Fig. 14. At the front face of mono-pile foundation, the embedment depth has minor
498 effect on liquefaction depth. The effect gradually increases as θ grows from approximately 30° to
499 180°: increasing embedment depth results in smaller liquefaction depth. It can be inferred that
500 increasing embedment depth has blocking effect on the pore water pressure propagation from front
501 face to back face of mono-pile foundation. As a result, the pore water pressure along the mono-pile
502 foundation with greater embedment depth presents slower reduction compared to that with smaller
503 embedment depth, which eventually decreases the difference of pore water pressure along the
504 embedment depth and leads to smaller liquefaction depth as shown in Fig. 14.

505

506 **5. Conclusions**

507 The numerical investigation of nonlinear wave-induced dynamic seabed response in the proximity of
508 mono-pile foundation has been performed in detail using one-way coupled solver in OpenFOAM. In
509 order to accurately describe the nonlinear wave interaction with mono-pile waves2Foam (Jacobsen et
510 al., 2012) is applied for the numerical simulation of flow field. In soil model, the quasi-static Biot
511 equations, solved by Finite Volume Method (Liu et al., 2007; Tang et al., 2015), govern the dynamic
512 response of porous seabed around mono-pile foundation. A coupled scheme, based on extended
513 general grid interpolation (GGI) (Tukovic et al., 2014) which allows the integrated model to run in
514 parallel, is used to integrate both sub-models. The comparisons with available laboratory
515 experimental results in the literature show excellent agreement for both wave and soil model. It
516 demonstrates that this integrated WSSI model is capable of estimating nonlinear wave-induced
517 mechanical behaviour of poro-elastic seabed around offshore mono-pile-supported structure.

518

519 The benefits of the present model compared to those so far presented in the literature are: (1)
520 nonlinear interaction of wave and mono-pile, including free surface elevation and inline force, is
521 predicted accurately; (2) the resulting wave-induced dynamic seabed behaviour near mono-pile
522 foundation is simulated simultaneously; (3) the associated momentary liquefaction potential in the

vicinity of mono-pile foundation can also be estimated based on available liquefaction criteria. The model at present does not incorporate poro-elasto-plastic soil model, nor the interaction between mono-pile foundation and seabed. These two mechanisms, which may result in different impacts on seabed response, also play vital roles in the assessment of offshore foundation stability and will be integrated into the future model.

The following conclusions are drawn from the present study:

(1) The wave-induced pore water pressure is weakened as soil depth increases. The presence of mono-pile foundation leads to the noticeably different distribution of pore water pressure in the vicinity of foundation. The vertical distribution of pore water pressure around mono-pile foundation varies significantly with θ: within a wave period, the range of pore water pressure reduces substantially between $\theta = 0°$ and $\theta = 90°$, and then gradually increases as θ grows from 90° to 180°. The range of pore water pressure at $\theta = 90°$ is the largest due to wave diffraction around mono-pile.

(2) Since pore water pressure within the seabed are attenuated compared to the pressures at seabed surface, the pressure difference between them generates an upward force resulting in the momentary liquefaction around mono-pile foundation. Application of a momentary liquefaction criterion shows that the horizontal distribution of liquefaction potential around mono-pile foundation (i.e. its variation with θ) is influenced by wave-pile interaction. Under the action of unidirectional regular waves with $KC = 8.85$ and $D/L = 0.032$, the maximum and minimum liquefaction depth take place at approximately $\theta = 90°$ and $\theta = 180°$, respectively. In a wave period, maximum liquefaction depth occurs at the positions with θ varying from 60° to 110°, where the scour protection may experience greater sinking compared to that at front and back sides of mono-pile foundation. However, since only one wave condition is taken into consideration, more investigations regarding various wave conditions are suggested to fully understand potential liquefaction around mono-pile foundation.

(3) Increasing embedment depth of mono-pile foundation significantly reduces the magnitude of pore water pressure along the embedded foundation, whereas the overall shape of the vertical pressure profiles remains similar. The increased blockage effect of larger embedment depths slightly reduces the difference of pore water pressure between the seabed and its surface, and hence also the corresponding liquefaction depth in the vicinity of the embedded mono-pile foundation.

Acknowledgements

The authors would like to acknowledge the financial support from Energy Technology Partnership (ETP), Wood Group Kenny, and University of Aberdeen. JH Zheng and JS Zhang would like to acknowledge the financial support from the National Science Fund for Distinguished Young Scholars (51425901) and the 111 project (B12032). The comments and suggestions provided by the anonymous Reviewers have greatly improved the quality of the final manuscript.

References

Bai, W., Taylor, R.E., 2007. Numerical simulation of fully nonlinear regular and focused wave diffraction around a vertical cylinder using domain decomposition. Applied Ocean Research, 29(1): 55-71.

Bai, W., Taylor, R.E., 2009. Fully nonlinear simulation of wave interaction with fixed and floating flared structures. Ocean engineering, 36(3): 223-236.

Berberović, E., van Hinsberg, N.P., Jakirlić, S., Roisman, I.V., Tropea, C., 2009. Drop impact onto a liquid layer of finite thickness: Dynamics of the cavity evolution. Physical Review E, 79(3): 036306.

Biot, M.A., 1941. General theory of three‐dimensional consolidation. Journal of Applied Physics, 12(2): 155-164.

Chang, K.-T., Jeng, D.-S., 2014. Numerical study for wave-induced seabed response around offshore wind turbine foundation in donghai offshore wind farm, shanghai, china. Ocean Engineering, 85: 32-43.

Chen, L., Zang, J., Hillis, A., Morgan, G., Plummer, A., 2014. Numerical investigation of wave–structure interaction using openfoam. Ocean Engineering, 88: 91-109.

Engsig-Karup, A.P., Bingham, H.B., Lindberg, O., 2009. An efficient flexible-order model for 3d nonlinear water waves. Journal of computational physics, 228(6): 2100-2118.

Eskesen, M., Buhrkall, J., Henningsen, J. (2010). 11761 - laboratoriepraktik. Technical report, Technical Universty of Denmark, Civil Engineering, Brovej, building 118, DK-2800 Kgs. Lyngby.

Hansen, NM, 2012. Interaction between Seabed Soil and Offshore Wind Turbine Foundations. Ph.D. thesis, Mechanical Engineering, Technical University of Denmark, Kgs. Lyngby, Denmark.

Higuera, P., Lara, J.L., Losada, I.J., 2013a. Realistic wave generation and active wave absorption for navier–stokes models: Application to openfoam®. Coastal Engineering, 71: 102-118.

Higuera, P., Lara, J.L., Losada, I.J., 2013b. Simulating coastal engineering processes with openfoam®. Coastal Engineering, 71: 119-134.

Higuera, P., Lara, J.L., Losada, I.J., 2014a. Three-dimensional interaction of waves and porous coastal structures using openfoam®. Part I: Formulation and validation. Coastal Engineering, 83: 243-258.

Higuera, P., Lara, J.L., Losada, I.J., 2014b. Three-dimensional interaction of waves and porous coastal structures using openfoam®. Part II : Application. Coastal Engineering, 83: 259-270.

Higuera, P., Losada, I.J., Lara, J.L., 2015. Three-dimensional numerical wave generation with moving boundaries. Coastal Engineering, 101: 35-47.

Hirt, C.W., Nichols, B.D., 1981. Volume of fluid (vof) method for the dynamics of free boundaries. Journal of computational physics, 39(1): 201-225.

Hsu, J.R.C., Jeng, D.-S., 1994. Wave-induced soil response in an unsaturated anisotropic seabed of finite thickness. International Journal for Numerical & Analytical Methods in Geomechanics, 18(11): 785-807.

Jacobsen, N.G., Fuhrman, D.R., Fredsøe, J., 2012. A wave generation toolbox for the open‐source cfd library: Openfoam®. International Journal for Numerical Methods in Fluids, 70(9): 1073-1088.

Jeng, D.-S., 2013. Porous Models for Wave–Seabed Interactions. Springer, Berlin Heidelberg, Germany.

Jeng, D.-S., 1997. Wave-induced seabed instability in front of a breakwater. Ocean Engineering,

24(10): 887-917.

Jeng, D.-S., 2003. Wave-induced sea floor dynamics. Applied Mechanics Reviews, 56(4): 407-429.

Jeng, D.-S., Ye, J.H., Zhang, J.S., Liu, P.L.F., 2013. An integrated model for the wave-induced seabed response around marine structures: Model verifications and applications. Coastal Engineering, 72(0): 1-19.

Jianhong, Y., Dongsheng, J., Liu, P.L.F., Chan, A. H. C., Ren, W., Changqi, Z., 2014. Breaking wave-induced response of composite breakwater and liquefaction in seabed foundation. Coastal Engineering, 85: 72-86.

Jianhong, Y., Dongsheng, J., Ren, W., Changqi, Z., 2013. Numerical study of the stability of breakwater built on a sloped porous seabed under tsunami loading. Applied Mathematical Modelling, 37(23): 9575-9590.

Kim, J., Kyoung, J., Ertekin, R., Bai, K., 2006. Finite-element computation of wave-structure interaction between steep stokes waves and vertical cylinders. Journal of waterway, port, coastal, and ocean engineering, 132(5): 337-347.

Kirby, J., Wen, L., Shi, F., 2003. Funwave 2.0 fully nonlinear boussinesq wave model on curvilinear coordinates. Center for Applied Coastal Research Dept. of Civil & Environmental Engineering, University of Delaware, Newark, USA.

Kirca, V.O., 2013. Sinking of irregular shape blocks into marine seabed under wave-induced liquefaction. Coastal Engineering, 75: 40-51.

Lesny, K., Paikowsky, S., Gurbuz, A., 2007. Scale effects in lateral load response of large diameter monopiles. Geotechnical Special Publication, 158: 1-10.

Li, X.-J., Gao, F.-P., Yang, B., Zang, J., 2011. Wave-induced pore pressure responses and soil liquefaction around pile foundation. International Journal of Offshore and Polar Engineering, 21(03):233–239

Liao, C., Jeng, D.-S., Zhang, L., 2013. An analytical approximation for dynamic soil response of a porous seabed due to combined wave and current loading. Journal of Coastal Research, 31(5): 1120-1128.

Lin, Z., Guo, Y., Jeng, D.-S., Liao, C., Rey, N., 2016. An integrated numerical model for wave–soil–pipeline interactions. Coastal Engineering, 108: 25-35.

638 Liu, B., Jeng, D.-S., Ye, G., Yang, B., 2015. Laboratory study for pore pressures in sandy deposit
639 under wave loading. Ocean Engineering, 106: 207-219.
640 Liu, X., García, M.H., Muscari, R., 2007. Numerical investigation of seabed response under waves
641 with free-surface water flow. International Journal of Offshore and Polar Engineering, 17(02).
642 Ma, Q., Wu, G., Eatock Taylor, R., 2001a. Finite element simulation of fully non‐linear interaction
643 between vertical cylinders and steep waves. Part 1: Methodology and numerical procedure.
644 International Journal for Numerical Methods in Fluids, 36(3): 265-285.
645 Ma, Q., Wu, G., Eatock Taylor, R., 2001b. Finite element simulations of fully non‐linear interaction
646 between vertical cylinders and steep waves. Part 2: Numerical results and validation.
647 International Journal for Numerical Methods in Fluids, 36(3): 287-308.
648 Madsen, O.S., 1978. Wave-induced pore pressures and effective stresses in a porous bed.
649 Geotechnique, 28(4): 377-393.
650 Mei, C.C., Foda, M.A., 1981. Wave-induced responses in a fluid-filled poro-elastic solid with a free
651 surface—a boundary layer theory. Geophysical Journal International, 66(3): 597-631.
652 Okusa, S., 1985. Wave-induced stresses in unsaturated submarine sediments. Geotechnique, 35(4):
653 517-532.
654 Paulsen, B.T., Bredmose, H., Bingham, H.B., 2014a. An efficient domain decomposition strategy for
655 wave loads on surface piercing circular cylinders. Coastal Engineering, 86: 57-76.
656 Paulsen, B.T., Bredmose, H., Bingham, H.B., Jacobsen, N.G., 2014b. Forcing of a bottom-mounted
657 circular cylinder by steep regular water waves at finite depth. Journal of Fluid Mechanics,
658 755: 1-34.
659 Qi, W.-G., Gao, F.-P., 2014. Physical modeling of local scour development around a large-diameter
660 monopile in combined waves and current. Coastal Engineering, 83: 72-81.
661 Shi, F., Dalrymple, R.A., Kirby, J.T., Chen, Q., Kennedy, A., 2001. A fully nonlinear boussinesq
662 model in generalized curvilinear coordinates. Coastal Engineering, 42(4): 337-358.
663 Sui, T., Zhang, C., Guo, Y., Zheng, J., Jeng, D.-S., Zhang, J., Zhang, W., 2015. Three-dimensional
664 numerical model for wave-induced seabed response around mono-pile. Ships and Offshore
665 Structures: 1-12.
666 Sumer, B.M., 2014. Liquefaction Around Marine Structures. World Scientific, New Jersey.

667 Sumer, B.M., Fredsøe, J., 2002. The Mechanism of Scour in the Marine Environment. World
668 Scientific, New Jersey.
669 Sumer, B.M., Fredsøe, J., 2006. Hydrodynamics Around Cylindrical Structures. World Scientific,
670 New Jersey.
671 Sumer, B.M., Hatipoglu, F., Fredsøe, J., 2007. Wave scour around a pile in sand, medium dense, and
672 dense silt. Journal of waterway, port, coastal, and ocean engineering, 133(1): 14-27.
673 Sumer, B.M., Hatipoglu, F., Fredsøe, J., Kaan Sumer, S., 2006. The sequence of sediment behaviour
674 during wave‐induced liquefaction. Sedimentology, 53(3): 611-629.
675 Swan, C., Sheikh, R., 2015. The interaction between steep waves and a surface-piercing column.
676 Philosophical Transactions of the Royal Society of London A: Mathematical, Physical and
677 Engineering Sciences, 373(2033): 20140114.
678 Tang, T., 2014. Modeling of soil-water-structure interaction. A finite volume method (FVM)
679 approach to fully coupled soil analysis and interactions between wave, seabed and offshore
680 structure. Ph.D. thesis, Technical University of Denmark, Kgs. Lyngby, Denmark.
681 Tang, T., Hededal, O., 2014. Simulation of pore pressure accumulation under cyclic loading using
682 Finite Volume Method. In Proceedings of 8th European Conference on Numerical Methods in
683 Geotechnical Engineering (NUMGE14). Taylor & Francis. pp. 1301–1306
684 Tang, T., Hededal, O., Cardiff, P., 2015. On finite volume method implementation of
685 poro-elasto-plasticity soil model. International Journal for Numerical and Analytical Methods
686 in Geomechanics, 39(13): 1410-1430.
687 Tukovic, Z., Cardiff, P., Karac, A., Jasak, H., Ivankovic, A., 2014. Openfoam library for fluid
688 structure interaction. 9th International OpenFOAM® Workshop, Zagreb, Croatia.
689 Wei, G., Kirby, J.T., 1995. Time-dependent numerical code for extended boussinesq equations.
690 Journal of Waterway, Port, Coastal, and Ocean Engineering, 121(5): 251-261.
691 Yamamoto, T., Koning, H.L., Sellmeijer, H., Hijum, E.V., 1978. On the response of a poro-elastic
692 bed to water waves. Journal of Fluid Mechanics, 87(01): 193-206.
693 Ye, J.-H., Jeng, D.-S., 2012. Response of porous seabed to nature loadings: waves and currents.
694 Journal of Engineering Mechanics. ASCE 138, 601–613
695 Ye, J., Jeng, D.-S., Chan, A., Wang, R., Zhu, Q., 2016. 3D integrated numerical model for fluid–

696 structures–seabed interaction (FSSI): Elastic dense seabed foundation. Ocean Engineering,
697 115: 107-122.
698 Ye, J., Jeng, D.-S., Wang, R., Zhu, C., 2013a. A 3-d semi-coupled numerical model for fluid–
699 structures–seabed-interaction (FSSI-CAS 3D): Model and verification. Journal of Fluids and
700 Structures, 40: 148-162.
701 Ye, J., Jeng, D.-S., Wang, R., Zhu, C., 2013b. Validation of a 2-d semi-coupled numerical model for
702 fluid–structure–seabed interaction. Journal of Fluids and Structures, 42: 333-357.
703 Ye, J., Jeng, D.-S., Wang, R., Zhu, C., 2015. Numerical simulation of the wave-induced dynamic
704 response of poro-elastoplastic seabed foundations and a composite breakwater. Applied
705 Mathematical Modelling, 39(1): 322-347.
706 Zang, J., Taylor, P.H., Morgan, G.C.J., Orszaghova, J., Grice, J., Stringer, R., Tello, M., 2010. Steep
707 wave and breaking wave impact on offshore wind turbine foundations–ringing re-visited. In
708 Proc. 25th International Workshop on Water Waves and Floating Bodies, Harbin, China.
709 Zhang, C., Zhang, Q., Wu, Z., Zhang, J., Sui, T., Wen, Y., 2015. Numerical study on effects of the
710 embedded monopile foundation on local wave-induced porous seabed response.
711 Mathematical Problems in Engineering, 2015: 1.
712 Zhao, H.-Y., Jeng, D.-S., Liao, C., 2016a. Effects of cross-anisotropic soil behaviour on the
713 wave-induced residual liquefaction in the vicinity of pipeline buried in elasto-plastic seabed
714 foundations. Soil Dynamics and Earthquake Engineering, 80: 40-55.
715 Zhao, H.-Y., Jeng, D.-S., Liao, C., 2016b. Parametric study of the wave-induced residual liquefaction
716 around an embedded pipeline. Applied Ocean Research, 55: 163-180.
717 Zhao, H.-Y., Jeng, D.-S., Guo, Z., Zhang, J.S., 2014. Two-dimensional model for pore pressure
718 accumulations in the vicinity of a buried pipeline. Journal of Offshore Mechanics and Arctic
719 Engineering, 136(4): 042001.
720

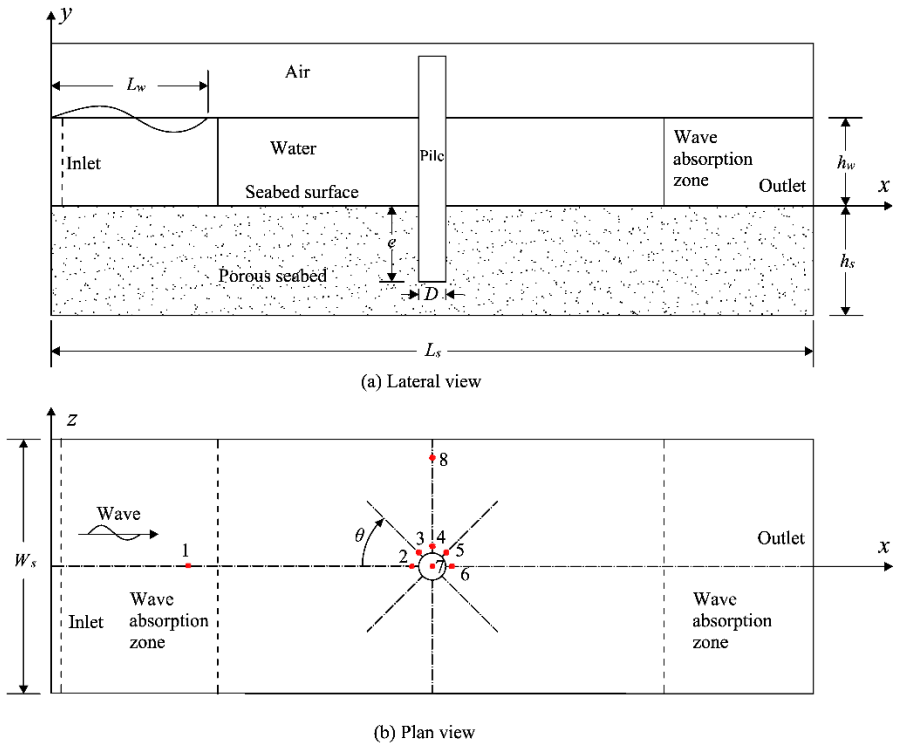

721

722 Fig. 1 Sketch of the numerical wave tank. (a) Lateral view, (b) Plane view; the red dots in plan view

723 are the locations of wave gauges or pressure sensors.

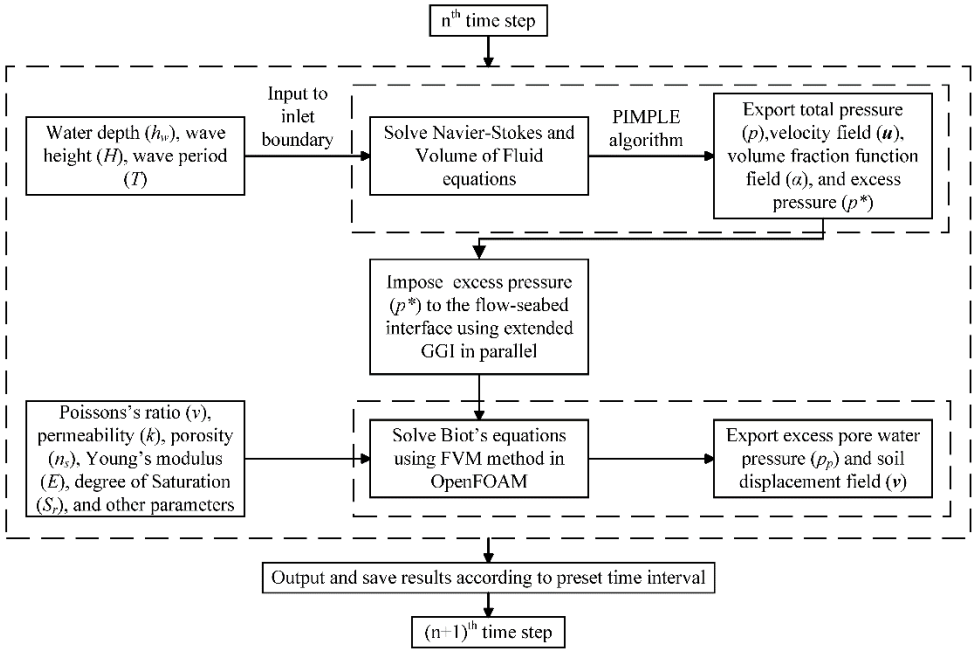

724

725 Fig. 2 Coupled processes in the integrated WSSI model in OpenFOAM

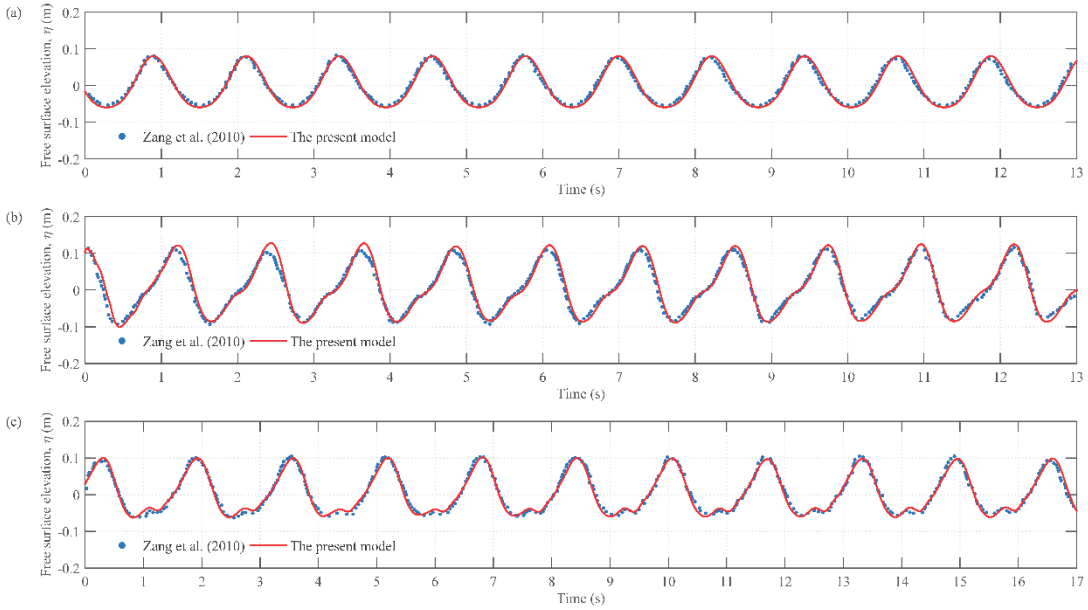

Fig. 1 Validation of free surface elevation (η) against experimental data (Zang et al., 2010). (a) Wave gauge 1 when H = 0.14 m and T = 1.22 s, (b) Wave gauge 2 when H = 0.14 m and T = 1.22 s, (c) Wave gauge 2 when H = 0.12 m and T = 1.63 s.

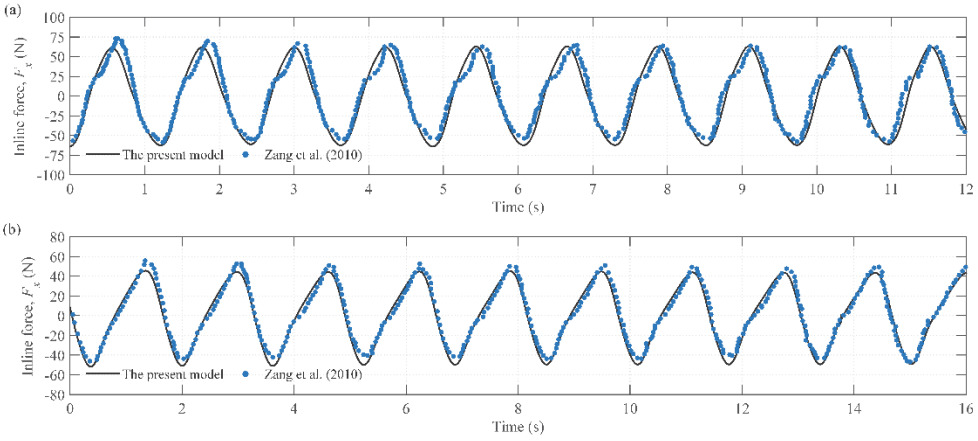

Fig. 2 Comparison of inline force (F_x) in OpenFOAM and experimental results (Zang et al., 2010). (a) H = 0.14 m and T = 1.22 s, (b) H = 0.12 m and T = 1.63 s.

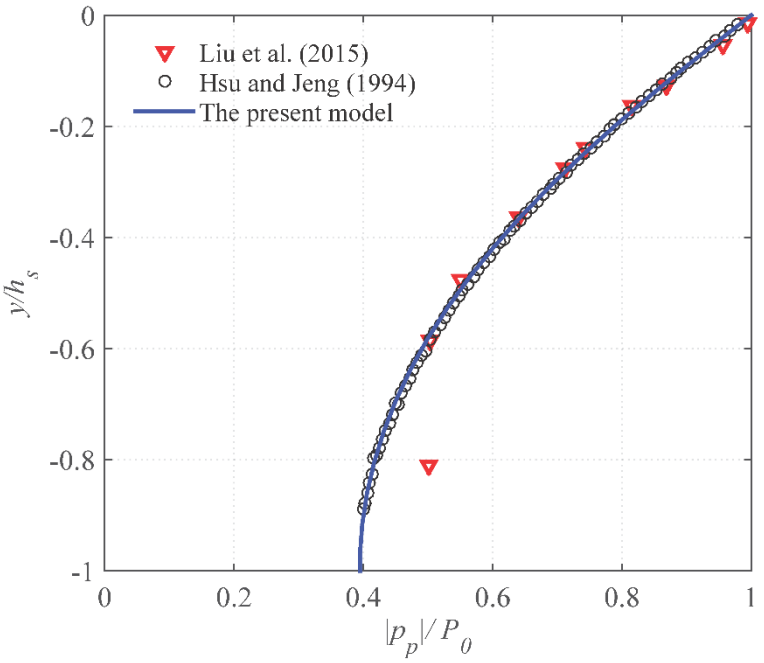

734

735 Fig. 3 Comparison of vertical distribution of maximum pore water pressure between laboratory
736 experiments from Liu et al. (2015) for S_r = 0.996 and numerical reproduction in OpenFOAM.
737

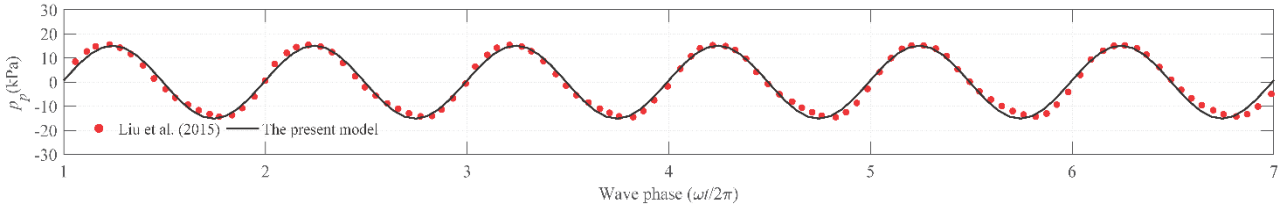

738
739 Fig. 4 Comparison of wave-induced pore water pressure p_p between the experimental data for S_r =
740 0.951 and numerical results in OpenFOAM at the depth y = -0.067 m (y/h_s=-0.037).
741

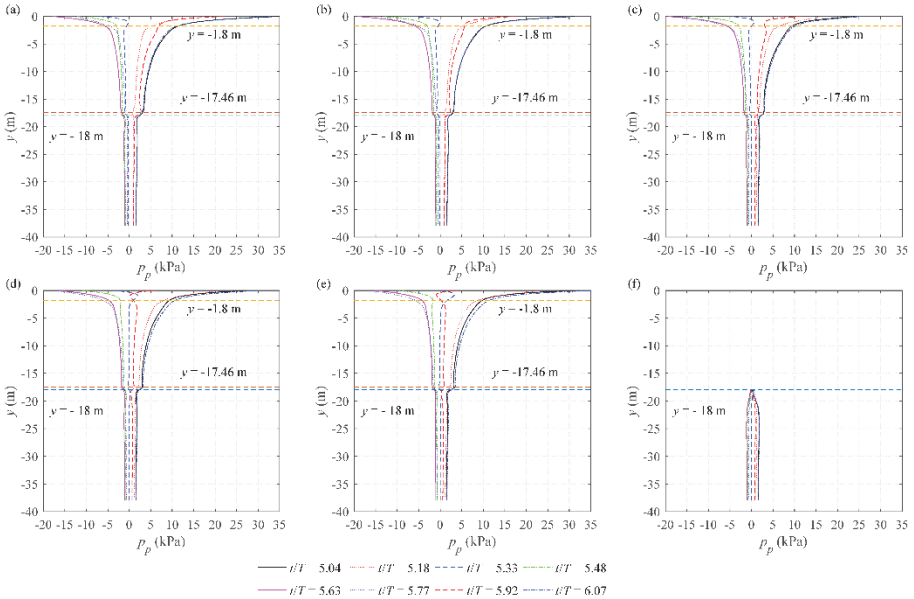

742
743
744 Fig. 5 Vertical distribution of pore water pressure at various positions. (a) θ = 0°, (b) θ = 45°, (c) θ =

90°, (d) θ = 135°, (e) θ = 180°, (f) Centre of mono-pile bottom.

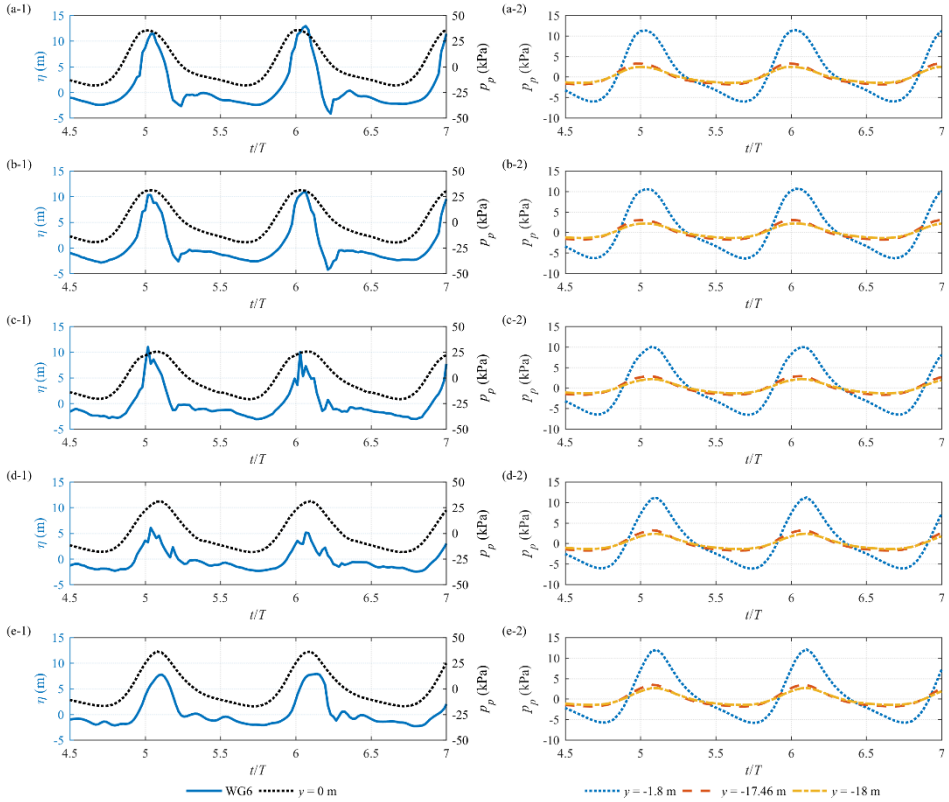

Fig. 6 Time series of free surface elevation (η) at various wave gauges. (a) θ = 0°, (b) θ = 45°, (c) θ = 90°, (d) θ = 135°, (e) θ = 180°. The first column are the comparisons of wave gauges and pore water pressure at y = 0 m. The second column are the comparisons of pore water pressure at y = -3 m, y = -17.46 m, and y = -18 m, respectively.

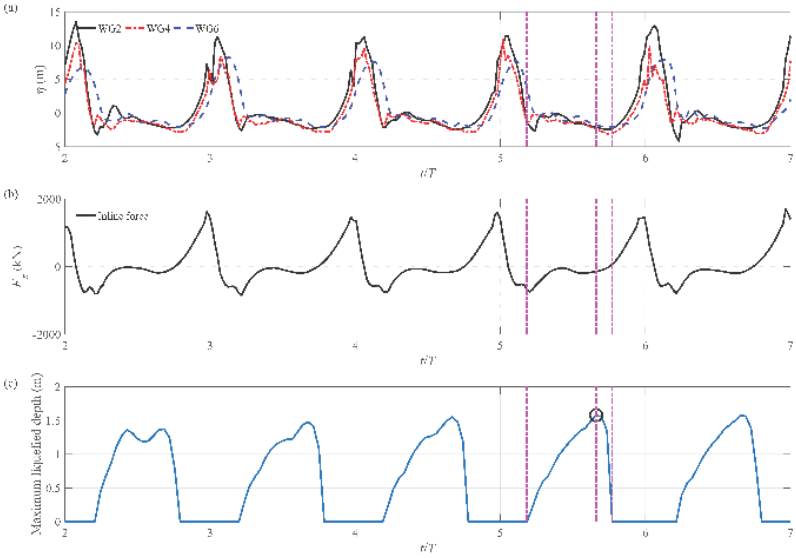

Fig. 7 Time series of (a) free surface elevation (η), (b) inline force, (c) maximum liquefied depth, with KC = 8.85 and D/L = 0.032.

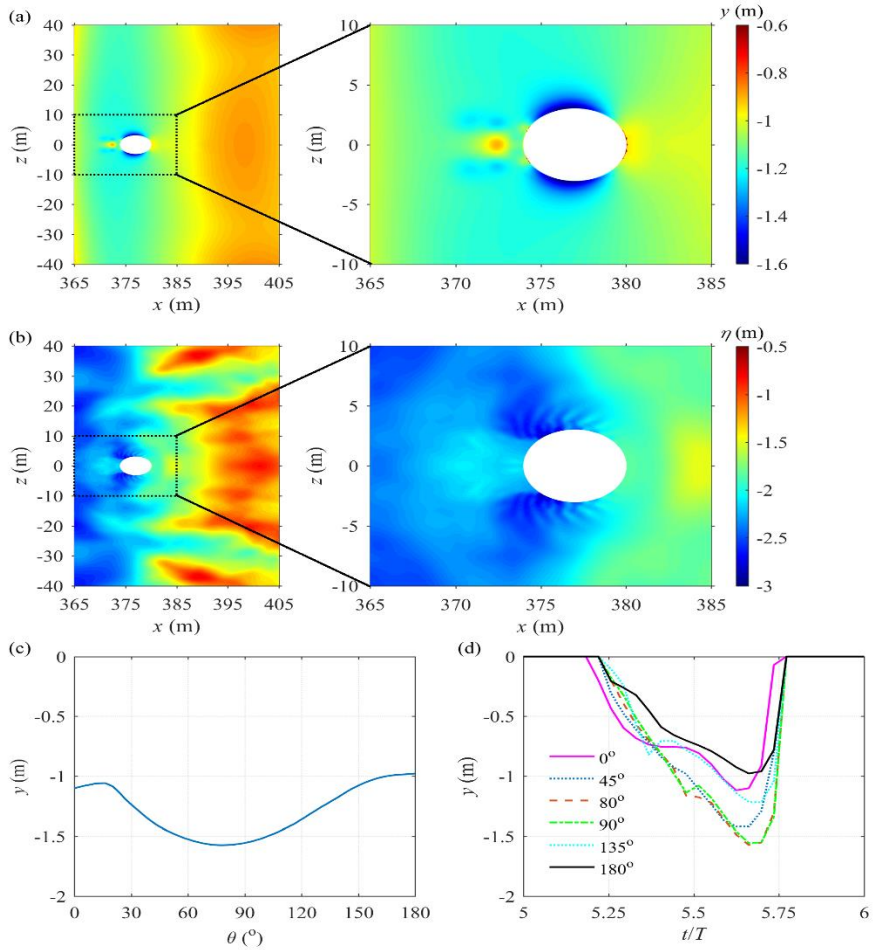

Fig. 8 Liquefaction depth (y) and free surface elevation (η) around mono-pile foundation at t/T = 5.66. (a) Contour plot of liquefied depth, (b) Contour plot of free surface elevation (η), (c) Liquefied depth for various θ–locations at the soil-pile interface, (d) Time series of liquefied depth at various θ-locations on the soil-pile interface.

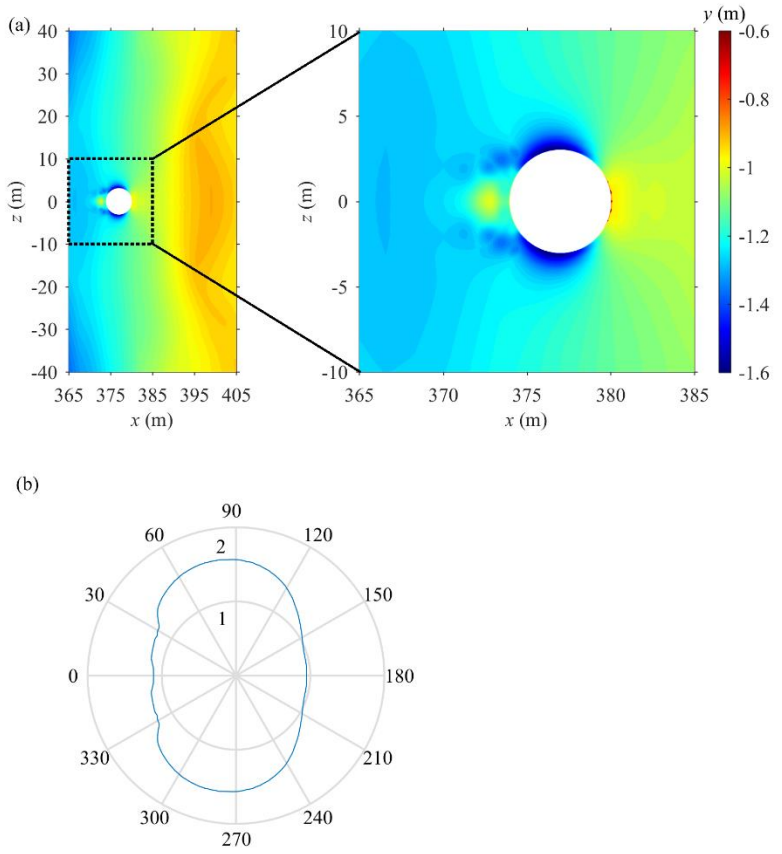

Fig. 9 Maximum potential liquefaction depth over a wave period (t/T from 5 to 6). (a) Horizontal distribution, (b) Maximum liquefaction depth varying with θ at the distance of 0.05m away from pile surface.

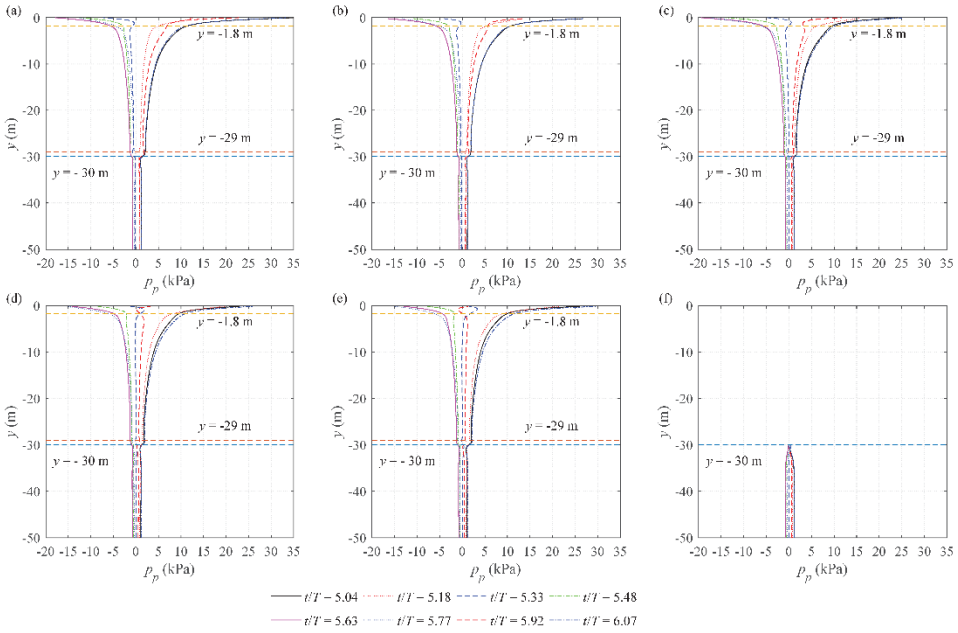

Fig. 10 Vertical distribution of pore water pressure at various positions when embedment depth e = 30 m. (a) θ = 0°, (b) θ = 45°, (c) θ = 90°, (d) θ = 135°, (e) θ = 180°, (f) Centre of mono-pile bottom.

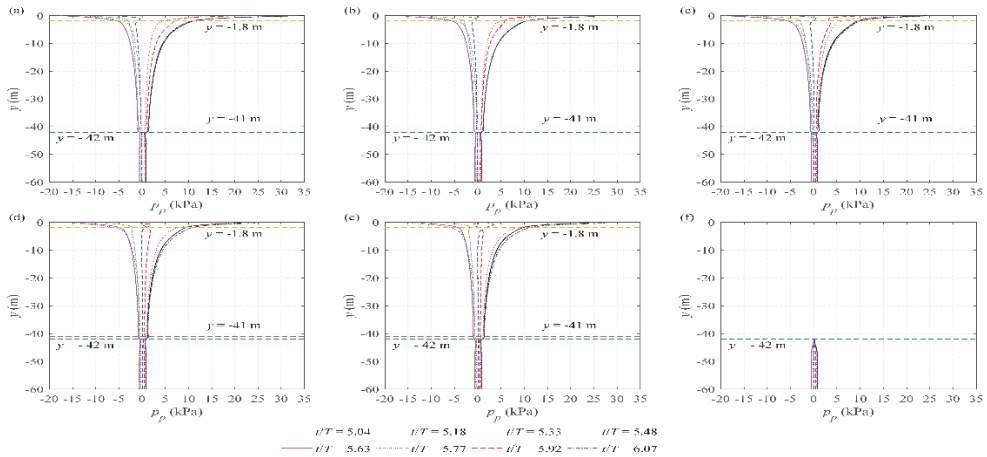

Fig. 11 Vertical distribution of pore water pressure at various positions when embedment depth e = 42 m. (a) θ = 0°, (b) θ = 45°, (c) θ = 90°, (d) θ = 135°, (e) θ = 180°, (f) Centre of mono-pile bottom.

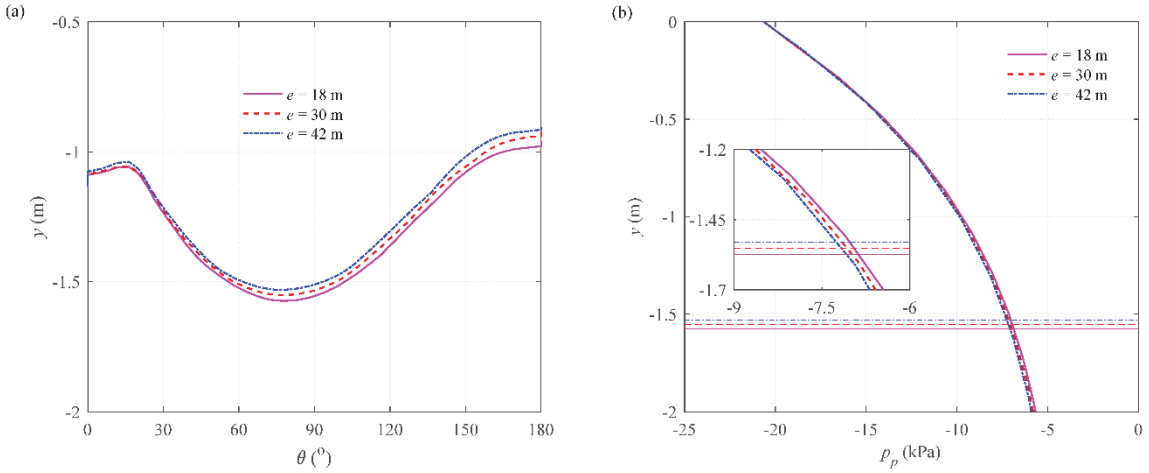

Fig. 12 Comparison of liquefied depth with various embedment depths at t/T = 5.66. (a) Spatial description of liquefied depth varying with θ on the soil-pile interface, (b) Liquefaction depth at θ =90°, horizontal lines are maximum liquefaction depth.

Table 1 Wave characteristics and soil properties for WSSI model validation

Experiments	H (m)	T (s)	h_w (m)	D (m)	e (m)	G (N/m^2)	υ	k (m/s)	n_s	S_r	h_s (m)
Zang et al. (2010)	0.14	1.22	0.505	0.25	0	0	0	0	0	0	0
	0.12	1.63	0.505	0.25	0	0	0	0	0	0	0
Liu et al. (2015)	3.5	9	5.2	0	0	1.27×10^{7}	0.3	1.8×10^{-4}	0.425	0.996	1.8
	3.5	9	5.2	0	0	1.27×10^{7}	0.3	1.8×10^{-4}	0.425	0.951	1.8

790 Table 2 Parameters for studying wave-seabed-pile interaction

Wave characteristics			
Wave height, H (m)	8.43	Wave period, T (s)	13.6
Water depth, h_w (m)	20	Wave length, e (m)	188.5
KC number	8.85		
Seabed characteristics			
Seabed thickness, h_s (m)	38, 50, 62	Poisson's ratio, ν	0.2
Submerged specific weight of sediment (kN/m^3)	9.5	Permeability, k (m/s)	1×10^{-4}
Degree of saturation, S_r	0.98	Soil porosity, n_s	0.38
Young's modulus	See section 4		
Mono-pile characteristics			
Diameter, D (m)	6	Embedment depth, e (m)	18, 30, 42
D/L	0.0032		

791